Design of Hybrid Airfoils for Icing Tunnel Tests Based on Reduced-Order Modeling Methods

Soonho Shon,[*] Yu-Eop Kang,[*] Yoonpyo Hong,[*] and Kwanjung Yee[†]

Seoul National University, Seoul 08826, Republic of Korea

and

R. S. Myong[‡]

Gyeongsang National University, Jinju 52828, Republic of Korea

Abstract

A hybrid airfoil is a scaled model used to generate a full-scale ice shape for icing wind tunnel tests. This is possible by matching full-scale properties such as the distributions of collection efficiency and heat transfer coefficient. Previous studies have used indirect methods using full-scale stagnation point location or tangent droplet trajectories. Therefore, these methods can cause a discrepancy between the full-scale and hybrid airfoil ice shapes under glaze ice conditions; this is because it is difficult to accurately match the distributions of full-scale collection efficiency and heat transfer coefficient. To improve accuracy, this paper proposes an approach to match the distributions of the full-scale collection efficiency and heat transfer coefficient on the leading edge, using a viscous turbulent CFD-icing simulation. For computational efficiency, reduced-order modeling (ROM) based optimization was used to match the distributions. The optimization design process was applied to the glaze ice condition with a high LWC and temperature. It is concluded that matching the distribution of the heat transfer coefficient is highly recommended to minimize the discrepancy between both ice shapes to obtain more reliable results from icing tunnel tests under the glaze ice condition. Further, by allowing separation, the hybrid airfoil achieves a more compact size than that designed without separation. Finally, a hybrid airfoil flap geometry, which can be applied to various angles of attack, was designed using the optimization design process. The ice shape of the hybrid airfoil with the flap yields good agreement with the full-scale ice shape.

---

[*] Graduate Student, Department of Mechanical and Aerospace Engineering.

[†] Professor, Department of Aerospace Engineering, Institute of Advanced Aerospace Technology; kjyee@snu.ac.kr. Member AIAA (Corresponding Author).

[‡] Professor, Department of Mechanical and Aerospace Engineering; myong@gnu.ac.kr. Associate Fellow AIAA.

Nomenclature

c_0	=	full-scale airfoil chord, m
c_{hybrid}	=	hybrid airfoil chord, m
h_c	=	heat transfer coefficient, $W/m^2 \cdot K$
LWC	=	liquid water content, g/m^3
MVD	=	median volumetric droplet diameter, μm
P	=	pressure, Pa
P_∞	=	freestream pressure, Pa
SF	=	hybrid scale factor, c_0/c_{hybrid}
T_∞	=	freestream static temperature, K
U_∞	=	freestream velocity, m/s
V	=	reconstruct vector
α	=	angle of attack, deg
α_j	=	POD coefficients
φ_j	=	POD modes
λ_j	=	POD eigenvalues
β	=	collection efficiency
δ	=	flap deflection angle, deg

I. Introduction

The Federal Aviation Administration (FAA) [1,2] provides aircraft certification regulations to certify aircraft airworthiness in icing conditions, as defined by the so-called icing envelope in the FAA's Federal Airworthiness Regulations (FAR) Part 25, Appendix C. All new aircraft must be designed and certified to demonstrate that it can fly safely for 45 min [3] in the icing envelope. The icing wind tunnel is one of the most important means of compliance to support the aircraft icing certification process and an attractive industry method owing to its capability to reproduce a controlled test matrix of icing conditions, which is relatively less expensive than icing flights.

However, icing wind tunnels have an inherent limitation whereby the size of the aircraft model is limited by the size of the test section of the existing facility. In particular, the wings of commercial transportation, which require actual certification, are several meters in size, impeding their testing in existing test sections. Therefore, proper scaling is required to test large wings in an existing icing wind tunnel. Scaling can be performed in two ways.

First is the geometrical scaling method, which reduces the size of the full-scale airfoil geometrically and adjusts the icing condition to maintain the icing similitude constant. However, it is difficult to use this method in icing tests as there is no complete set of dimensionless parameters that account for the flow field and also heat convection, conduction, evaporation, and other features. [4–9].

The second method is to use a hybrid airfoil, which does not have to consider geometrical similitude. The hybrid airfoil is designed by maintaining the same leading-edge geometry of the full-scale airfoil, where icing occurs, and reducing the aft section without scaling the icing condition, as shown in Fig. 1. The reduced airfoil is called a hybrid airfoil and the hybrid scale factor [10] is defined as the ratio of the full-scale airfoil chord to the hybrid airfoil chord. A hybrid airfoil can generate the same full-scale ice accretion by properly designing an aft section to form a full-scale flow field, droplet impingement, and thermodynamic characteristics in the leading-edge region. The hybrid airfoil is usually susceptible to separation owing to the reduced aft section. To reduce or suppress the separation, flap is sometimes used, and which enables hybrid airfoil to be applied at multiple angles of attack.

In the 1950s, research on hybrid airfoils began by Von Glahn [11], who experimentally demonstrated that a hybrid airfoil with a truncated flap can simulate full-scale ice accretion. Various studies [12–14] have been experimentally and analytically conducted using hybrid models to test the full-scale ice protection system of a wing section. In the late 1990s, Saeed et al. [10] first proposed a numerical design method for hybrid airfoils. Ice

usually accretes only on the airfoil leading edge, and hence a hybrid airfoil was designed with the same leading-edge geometry as the full-scale airfoil, where the supercooled water droplets impinge. Then, the aft section was designed to provide full-scale droplet impingement on the leading edge by indirect method matching full-scale tangent droplet trajectories [10]. A flap was also used for the aft section to make a hybrid airfoil possible to be applied at multiple angles of attack [15,16]. The study concluded that ice shapes could be matched by matching only the flow field and droplet impingement between the full-scale and hybrid airfoils; however, they could not compare the actual ice accretion due to the absence of an ice accretion analysis tool.

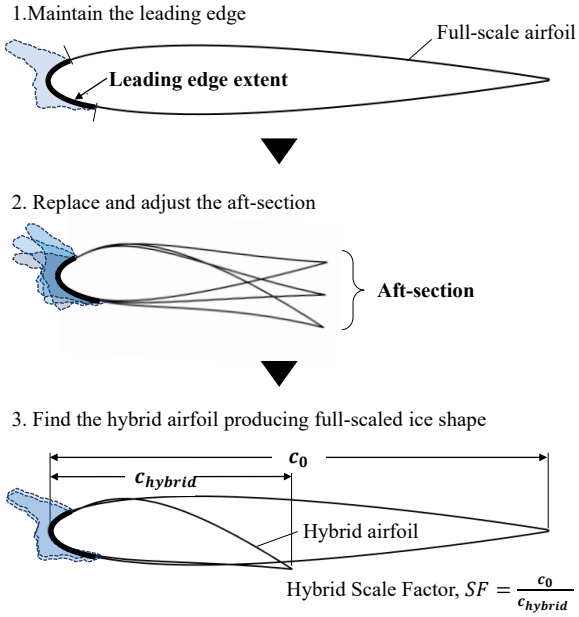

Fig. 1 Definition of hybrid airfoil

Recently, by using ice accretion analysis code NASA LEWICE [20], Fujiwara et al. [17–19] presented a novel design process, as shown in Fig. 2, to validate the agreement of ice shapes between full-scale and hybrid airfoils. First, the hybrid airfoil geometry was defined as demonstrated by Saeed et al. [10] and the optimal design of the hybrid airfoil was obtained through the inverse airfoil design method. To that end, the hybrid airfoil was designed to match the full-scale stagnation point location through an iterative process. The hybrid airfoil was then evaluated with a 2-D RANS solver to check for acceptable flow separation, which affects the stagnation point location. This was because LEWICE is based on an inviscid panel code that cannot consider the viscous effects of separation. Finally, by comparing the ice accretions between the full-scale and hybrid airfoils, the study concluded that

matching the full-scale stagnation point location is key design parameter for matching the full-scale ice accretion and collection efficiency.

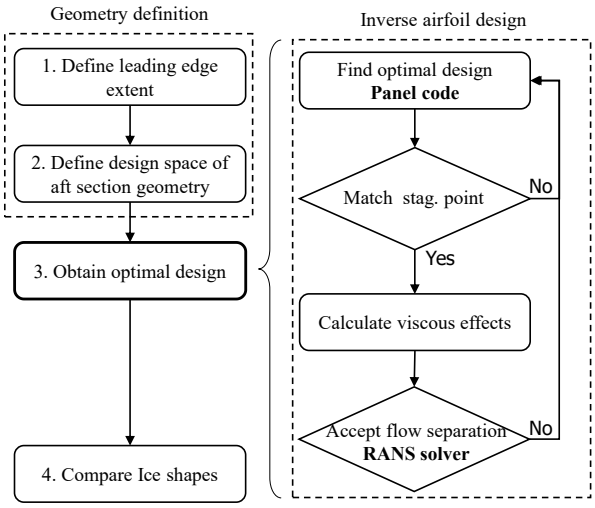

Fig. 2 Flow chart of hybrid airfoil design [17-19]

Although the studies [17–19] presented a parameter for hybrid airfoil design to match the full-scale ice accretion, the same limitations remain when reviewing previous hybrid airfoil studies.

First, matching only the full-scale droplet trajectories or stagnation point does not accurately match the variation in convective heat transfer which can result from the difference in aft sections. While various energies, such as droplet kinetic energy and evaporation energy, are involved in ice accretion, convective heat transfer has a dominant influence [21]. Therefore, the difference in ice shapes can be caused by inconsistencies in convective heat transfers between the full-scale and hybrid airfoils. In particular, a significant difference in ice shapes (e.g., ice horn angle and ice horn thickness) may occur in the glaze ice conditions of high liquid water content (LWC) and temperature.

Second, the use of the inviscid panel code provided a constraint that separation should not occur on the hybrid airfoil. As explained earlier, the hybrid airfoil has a shorter aft section than the full-scale airfoil, and thus tends to cause separation. Therefore, designing the hybrid airfoil so that separation does not occur is an excessive constraint on the design space. This impedes the design of a more compact hybrid airfoil.

Third, there is no general method for designing hybrid airfoil flap geometries. Research on flap reducing separation [17] has mainly been conducted. Although a flap was also used in the hybrid airfoil to generate a full-scale ice shape at multiple angles of attack [18,19], shape parameters — such as flap geometry, main section, gap,

and overlap — were set arbitrarily. When the method of designing the flap geometry is not specific, it is difficult to design an optimal flap geometry to achieve an accurate full-scale ice shape.

To overcome the limitations of previous studies, this study attempts to provide a general method for designing a compact hybrid airfoil, which can be applied to glaze ice conditions where even LWC and temperature are high in the icing envelope. A novel method is suggested to achieve this goal.

First, to consider the accordance of convective heat transfer, the distribution of the full-scale heat transfer coefficient (h_c) is matched. In addition, this study matches the distribution of full-scale collection efficiency (β) directly as well as the full-scale stagnation point used in previous studies. From this, the hybrid airfoil can yield good agreement with the full-scale ice shape by evaluating quantitatively the total difference distributions of collection efficiency (β) and heat transfer coefficient (h_c) between both airfoils. For computational efficiency, reduced-order modeling (ROM)-based optimization is applied to match the distributions. Second, to relax the separation constraint, a viscous turbulent CFD-icing simulation is used instead of an inviscid panel code. From this, variations in the flow field due to separation can be directly reflected in the CFD process without having to check whether the separation occurs in design process. Furthermore, it is possible to design a compact hybrid airfoil by allowing separation. Third, a general method for designing flap geometry is suggested, which can be applied to various angles of attack. The main section and flap geometry are defined using the Bezier curve, and are obtained through an optimization process to generate an accurate full-scaled ice shape.

The remainder of this paper is organized as follows: In the next section, the overall optimization design process of the hybrid airfoil is explained. In Section III, a newly suggested methodology is applied for a glaze ice condition, and the results are thoroughly discussed. Finally, a conclusion is presented.

II. Design Optimization Process

The hybrid airfoil design process presented in this study is shown in Fig. 3. The design process comprises four main steps, which are similar to the method of Fujiwara et al. [17–19]. Step 1 is to find the points that determine the leading-edge extent of the hybrid airfoil by obtaining the icing limit or impingement limit of the full-scale airfoil. In step 2, the design variables and design space are defined. In step 3, the optimal design of the hybrid airfoil is obtained to generate a full-scale ice shape. Finally, the accuracy between ice shapes of the full-scale and hybrid airfoils are evaluated in step 4, through ice accretion simulation.

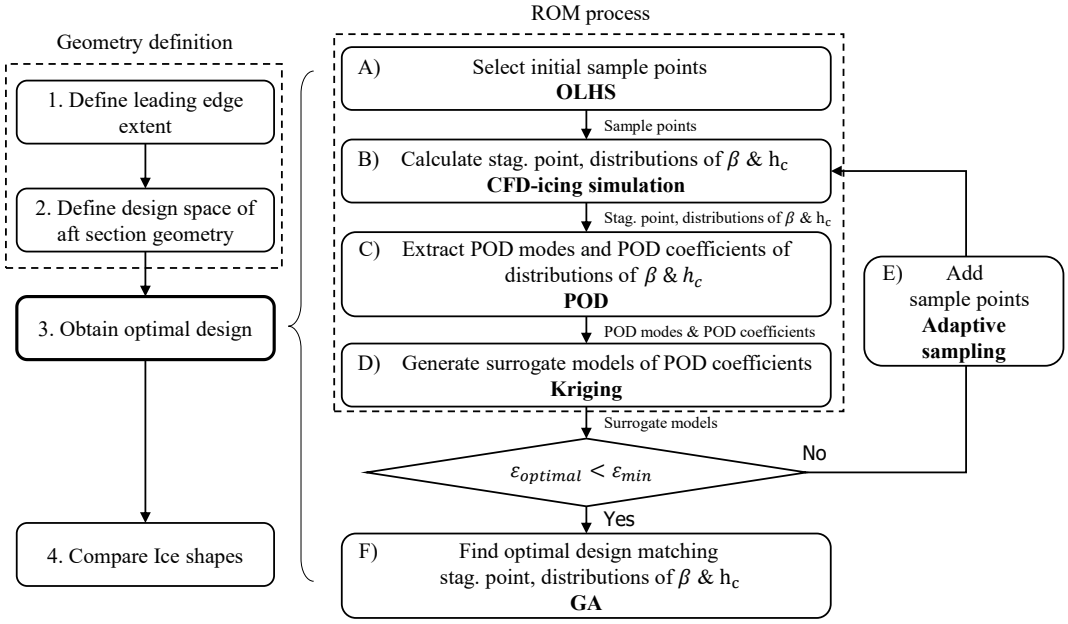

Fig. 3 Flow chart of the optimization design process

In this study, reduced-order modeling (ROM)-based optimization was used to optimally design a hybrid airfoil, as in step 3. This was chosen for the following reasons: In previous studies [17–19], the method of matching the full-scale stagnation point was used for the hybrid airfoil design. In this study, to consider convective heat transfer, the distribution of the full-scale heat transfer coefficient (h_c) is also matched. In addition, the distribution of full-scale β is directly matched, instead of indirect methods. Therefore, the hybrid airfoil can yield good agreement with the full-scale ice shape by computing the total difference distributions of β and h_c between both airfoils. To obtain the distributions, a viscous turbulent CFD-icing simulation which is a high-fidelity solver, was used. However, the use of high-fidelity in an iterative procedure can be prohibitively expensive. Therefore, a surrogate model that offers a good approximation of the entire solution at reduced computational costs is used. In addition, because the distributions of β and h_c comprise data for the several nodes existing on the leading-edge surface, they are not a single scalar value but a vector that is high-dimensional data. It requires a huge computational cost to generate a surrogate model for each element of the vector directly. For computational efficiency, reduced-order modeling (ROM) is used based on proper orthogonal decomposition (POD) [22].

The ROM approach uses a set of simulation outputs (called snapshots) obtained at inputs in the parametric space to obtain a basis of vectors (also called modes) which optimally spans the simulation's output space. POD is a popular technique for finding the orthonormal basis vectors (also called POD modes), which form the basis on

which each snapshot can be expressed as a linear combination. POD also has the advantage of being able to represent most of the information with truncated modes. In this study, the POD modes (φ_j) of β and h_c are extracted and the POD coefficients (α_j) are obtained projecting the snapshots (β and h_c) onto the POD modes. Figure 4 schematically shows that the snapshots can be reconstructed from a combination of POD modes and coefficients when the snapshots (β and h_c) of the sample points ($i = 1, \dots, N_s$) of random design variables 1 and 2 are obtained. The reconstructed vector (V) is calculated using Eq. (1):

$$V = \sum_{j=1}^{M<N_p} \alpha_j \varphi_j \tag{1}$$

M indicates the minimum number of modes required to indicate the energy content, which is the ratio of the energy required for the total energy, and N_p is the number of nodes that ma

ke up the distribution of β and h_c. POD is introduced in detail in [23,24], and POD studies of icing have been extended and applied in [25–28].

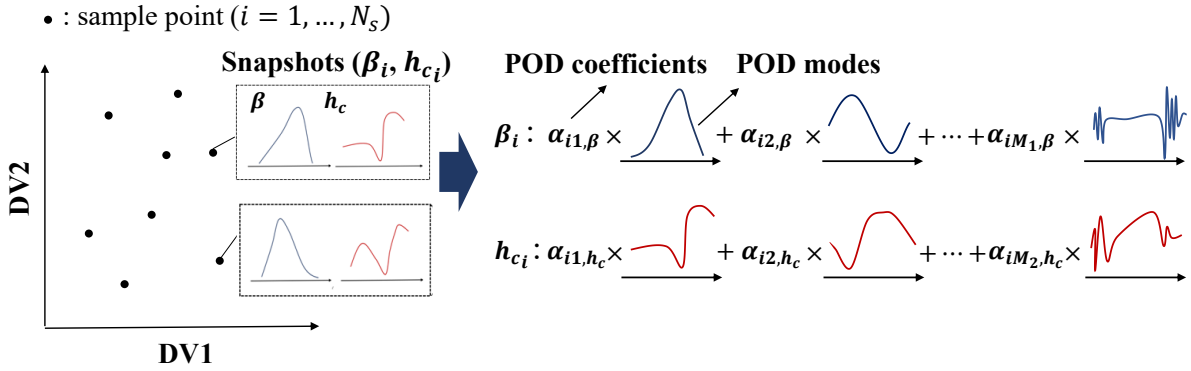

Fig. 4 Reconstruction of β and h_c by POD modes and POD coefficient

The optimization process using POD-based ROM, as shown in Fig. 3, consists of the following steps: In step A, the initial sample points are selected as the design of experiment (DOE) [27] by optimal Latin hypercube sampling (OLHS) [30]. In step B, a viscous turbulent CFD-icing simulation is used to obtain the stagnation point location and distribution of β and h_c for the selected sample points. In step C, the POD modes and POD coefficients of β and h_c are extracted. In step D, the response surface for the POD coefficients is obtained by kriging [31]. In step E, to improve the accuracy of the ROM, adaptive sampling [32] is used and sample points are added repeatedly until the error between the CFD and ROM prediction satisfies the minimum error. The details of

adaptive sampling are provided in the Appendix. Finally, the optimal design of the hybrid airfoil is obtained using a genetic algorithm (GA) to satisfy the error of the stagnation point and distributions of β and h_c between full-scale and hybrid airfoils.

In this section, the design variables required to define the hybrid airfoil geometry are presented and the optimization problem is defined by determining the objective functions and constraints. Finally, the CFD icing analysis tools used in this study are briefly presented.

A. Geometry definition

In this section, the first step (define leading-edge extent) and the second step (define design space of aft section geometry) of the design process are introduced and the flap geometry is defined.

First, the minimum range of the leading-edge extent is determined by calculating the icing limit of the full-scale airfoil via icing analysis. In a previous study [17], the impingement limit was selected to determine the extent of the leading edge. However, because the icing limit is larger than the impingement limit in the glaze ice condition due to water runback, the icing limit is set as the minimum point of the leading-edge extent in this study.

The Bezier curve is used to design the aft section, as shown in Fig. 5. The Bezier curves are defined by nine Bezier points ($P_i, i = 1, \dots, 9$) which are adjusted via a total of seven design variables ($V_j, j = 1, \dots, 7$). Only the minimum design variables are intuitively selected to represent the geometrical properties of the hybrid airfoil. The geometrical properties of each design variable are as follows: to define the chord length and the elevation of the tailing edge, V_1 and V_2 are adjusted in the x- and y- directions, respectively. The curvatures of the aft section are controlled by V_3 and V_4, respectively, in the y- direction. The thickness of the hybrid airfoil is mainly defined by V_5, adjusting the movement of P_3, P_4, P_7, and P_8 in the x- direction. Finally, the leading-edge extent is extended by V_6 and V_7, which adjusts P_5 and P_6, respectively, for the upper and lower sides of the hybrid airfoil.

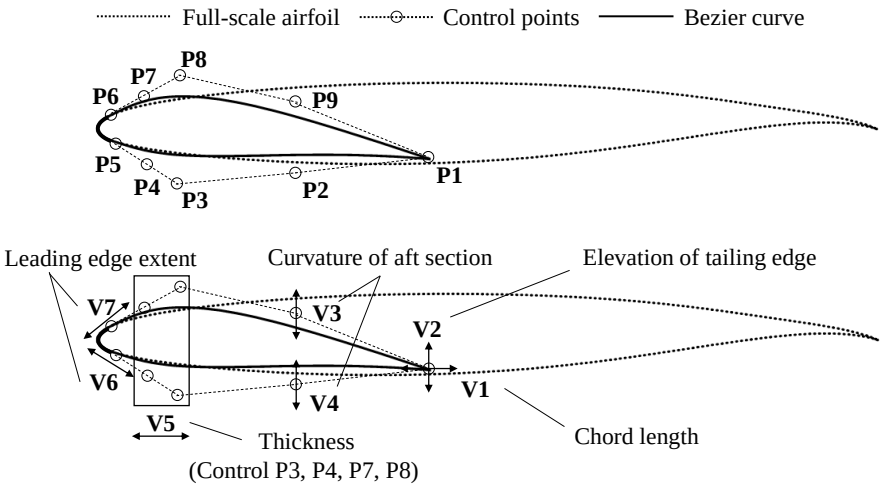

Fig. 5 Hybrid airfoil parameters definition

The geometries of the main section and flap are also designed using the Bezier curve, as shown in Fig. 6, and are constructed based on the reference geometry. First, the reference geometry is a single hybrid airfoil designed at an angle of attack of zero, and its leading-edge extent includes all icing ranges of the full-scale airfoil, calculated at the desired angle of attack range. For the main section and flap, 14 Bezier points $(P_i, i = 1, \dots, 14)$ and five design variables $(V_j, j = 1, \dots, 5)$ are used and the design space is selected to satisfy the continuity and manufacturing characteristics of the flap. The gap and overlap, which are the most important factors in the flap design, and shape of the flap, including the length of the lip and leading-edge location, can be determined through the set design variable for geometry. The flap deflection angle and angle of attack are adjusted by V_6 and V_7. Therefore, a total of seven variables are used in the optimization.

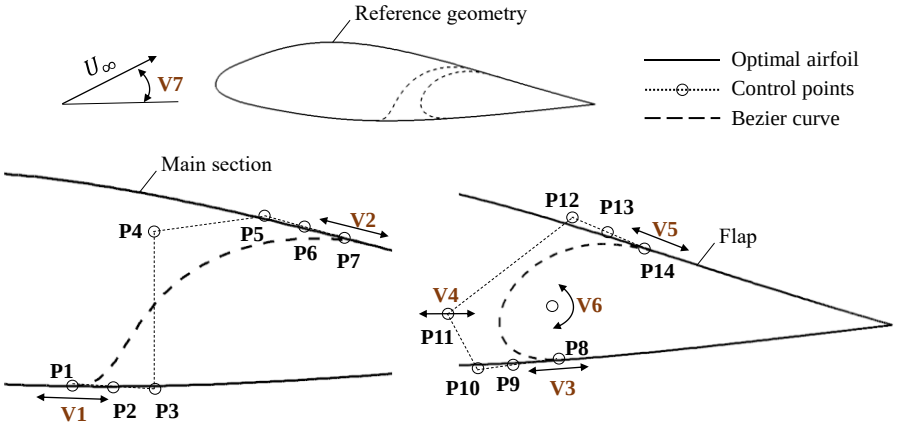

Fig. 6 Main section and flap parameter definition

220 **B. Optimization problem**

221 For the global optimum [33], GA, which has the advantage of being robust in even a complex and nonlinear
222 system, is selected. It is necessary to determine the objective function and constraints when deriving the optimal
223 design. In this study, a major concern in the design of a hybrid airfoil is to find an optimal hybrid airfoil with a
224 compact size, which has the full-scale stagnation point location and distribution of β and h_c. Considering of this
225 issue, one objective function and four constraints are defined. The optimization problems are formulated as
226 follows:

$$\text{minimize} \quad f(x) \ \ (f(x) \text{ is the chord length}) \tag{2}$$

$$\text{subject to} \quad x \notin \Omega \ \ (\Omega \text{ is the unsteadiness region}) \tag{3}$$

$$\Delta n \leq 1 \ \ (\Delta n \text{ is the index difference of stagnation point locations}) \tag{4}$$

$$\varepsilon_{\beta(x)} < \varepsilon_{min,\beta} \tag{5}$$

$$\varepsilon_{h_{(x)}} < \varepsilon_{min,h_c} \tag{6}$$

where

$$\varepsilon = \int_{LE} \left| U_{full} - V_{hybrid} \right| ds \Big/ \int_{LE} U_{full} ds \ \ (U, V \in \mathbb{R}^{N_p}) \tag{7}$$

227 The objective function is to minimize the chord length (denoted as $f(x)$) of the hybrid airfoil while satisfying
228 the constraints. These constraints can be classified into two categories.

229 The first is that design variables x must not exist in the region where unsteadiness occurs (denoted as Ω) due
230 to separation. This is because unsteadiness affects the boundary layer of the leading edge (if it occurs) and
231 distribution of h_c fluctuates with time; thus, it becomes difficult to numerically predict the shape of ice. In
232 addition, tunnel blockage can be experimentally increased. Therefore, it is necessary to prevent unsteadiness from
233 occurring when separation is allowed. The unsteadiness can be determined by performing a steady flow-field
234 analysis.

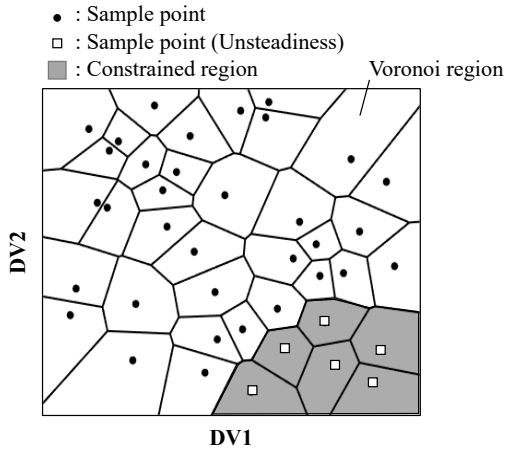

Fig. 7 Definition of constrained region through Voronoi tessellation

In this study, when the CFL number is set to 2 and the flow field is calculated 30,000 times or more, if the residual of density does not decrease to 10^{-4} or if it does not maintain a constant value, unsteadiness is judged to occur. When unsteadiness occurs at sample points, the constrained region is defined through the concept of Voronoi tessellation [34], which is a subdivision of the space into n cells, given sample points ($P_i, i = 1, \dots, n$), by using the Euclidean distance from the points. The Voronoi regions of the sample points where unsteadiness occurs are constrained, if random design variables 1 and 2 are set as shown in Fig. 7. Constrained regions must not be selected in the optimization process or adaptive sampling.

The second category of constraints is defined to match the ice shapes between the full-scale and hybrid airfoils. First, the difference index of the stagnation point locations (Δn) between the full-scale and hybrid airfoils is 1 or less. Second, the differences area ($\varepsilon = \int_{LE} |U_{full} - V_{hybrid}|\, ds \Big/ \int_{LE} U_{full} ds$, U: CFD vector, V: reconstruct vector) of the distributions of β and h_c between both airfoils on the leading edge extent (LE) are smaller than the minimum errors ($\varepsilon_{min,\beta}$ and ε_{min,h_c}), respectively. The distributions of β and h_c are calculated by the nodes ($i = 1, \dots, N_p$), distributed on the leading-edge extent, which are at the same location for all airfoils.

C. CFD-icing solver

The CFD-icing solver consists of four sequentially coupled modules [33]: aerodynamics, droplet trajectory, thermodynamics, and generation of ice shapes. For the flow field, compressible steady Reynolds-averaged Navier-Stokes equations in KFLOW [38] is used, where the finite volume method (FVM) is used. For the turbulence

model, the modified Spalart-Allmaras model [39], which considers the surface roughness, is selected. Roe's approximate Reimann solver is applied to perform the convective term, and the TVD MUSCL limiter is also applied to improve the accuracy of the flow field. For the icing analysis simulation, the Ice Contour Estimation and Performance Analysis Code (ICEPAC) [33–35] is used. The droplet trajectory and thermodynamic modules are constructed based on all PDEs, and a description of the equations can be found with reference to [35]. The HLLC approximate Riemann solver [40–42] is applied to perform the convective term of the droplet equation. For the thermodynamics module, 1st order upwind is applied for the convective term. The validation of ICEPAC proceeds with reference to the NASA icing tunnel test [43]. Comparisons of the ice shapes between the simulation and experiment for the cases listed in Table 1 are shown in Fig. 8. It is confirmed that the icing solver used in this study accurately predicts the angle of the ice horn and the size of the overall ice shape.

Table 1 Validation condition [43]

Case name	A	B	C
$Airfoil$		NACA0012	
$Chord\ length, m$		0.5334	
α, deg		4	
$V_\infty, m/s$		102.8	
$LWC, g/m^3$	0.55	0.55	1.0
$MVD, \mu m$	20	20	20
$Temperature, K$	262.04	250.37	262.04
$Times, s$	420	420	231
$NASA\ IRT\ case\ No$	403	405	308

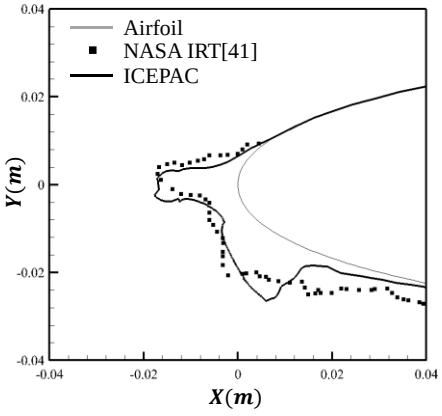

a) Case A ($V_\infty = 102.8m/s$, LWC $= 0.55g/m^3$, MVD $= 20\mu m$, $T_\infty = 262.04K$, $\alpha = 4°$)

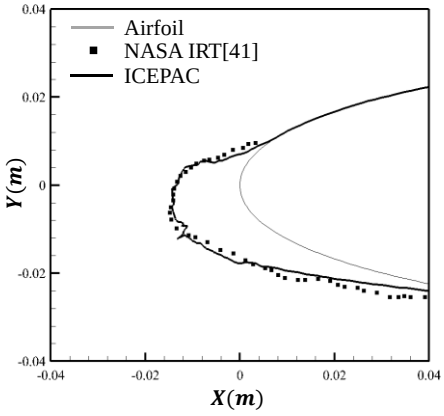

b) Case B ($V_\infty = 102.8m/s$, LWC $= 0.55g/m^3$, MVD $= 20\mu m$, $T_\infty = 250.37K$, $\alpha = 4°$)

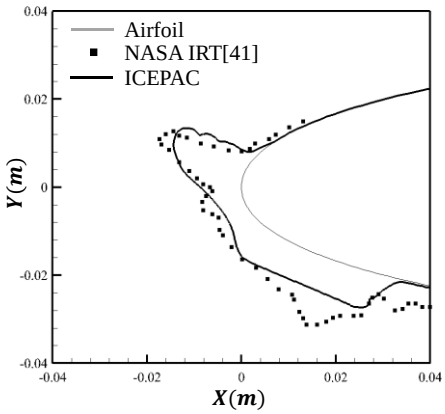

c) Case C ($V_\infty = 102.8m/s$, LWC $= 1.0g/m^3$, MVD $= 20\mu m$, $T_\infty = 262.04K$, $\alpha = 4°$)

Fig. 8 Predicted shapes of ice compared with those of the NASA IRT cases [43]

그림 속 [41] -> [43]

III. Results & Discussion

In this section, the design optimization process is applied to an actual problem. For reference geometry, CRM 65, which is 65 % scaled from the common research model (CRM) [44], is used, and CRM 65 is similar in size to the B757-200. A 2D full-scale airfoil can be obtained in the vertical cross-section of the leading edge of the CRM wing. The position of the cross-section is spanwise 60 %, corresponding to the outboard wing section. The length of the full-scale airfoil is 3.07m and the tailing edge of the airfoil, where the twist angle exists, is positioned at y=0. This airfoil is used in all parts of this section as a full-scale airfoil.

The remainder of this section is organized as follows: In the next section, the overall optimization design process, applied to the icing condition as listed in Table 2, is presented. Second, the necessity of matching the distributions of heat-transfer coefficient and collection efficiency is presented. Third, the optimization results are analyzed to show the benefits of allowing separation. Finally, the results of the hybrid airfoil flap design are presented, demonstrating the validity of the design method.

A. Results of the design process

The purpose of this study is to present a general method for designing compact hybrid airfoil, which can be

applied to glaze ice conditions with high LWC and temperature. In consideration of the purpose, the glaze ice condition listed in Table 2 (in the FAR Part 25 Appendix C intermittent maximum condition) is chosen, as shown in Fig. 9. The ice condition is condition where a critical ice horn occurs and is selected to show that it is possible to design a hybrid airfoil through the method presented herein, even under critical conditions. For numerical analysis, an O-type grid is used and all hybrid airfoils consists of 396 surface grids with 0.0001 spacing on the leading edge to make it sufficiently dense.

Table 2 Test case for hybrid airfoil design

Parameter	Value
α, deg	2
$V_\infty, m/s$	102.8
$Times, s$	960
$LWC, g/m^3$	2.4
$MVD, \mu m$	18
$Temperature, K$	263.15

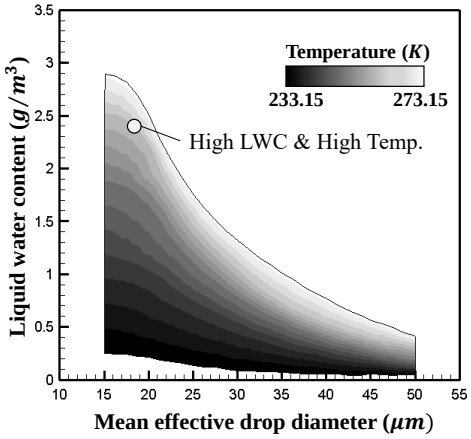

Fig. 9 Test cases on FAR 25 Appendix C [2]

ICEPAC is used to predict the ice shape and icing limit of a full-scale airfoil to determine the leading-edge extent for the hybrid airfoil. The design space of the aft section is defined as having a chord length of 0.5 ~ 2 m and the thickness should not exceed the full-scale airfoil thickness. Using OLHS, 70 initial sample points for seven design variables are selected to construct the ROM. From the sampling points, the distributions of β and h_c, which comprises outputs from 196 nodes on the leading-edge extent, are calculated using KFLOW and ICEPAC. Then the POD method is implemented on the data to determine the POD modes required to accurately represent the snapshots (β and h_c). Through the eigenvalue of modes ($i = 1, \dots, N_p$), the ratio of each mode to the total energy

can be formulated as follows:

$$E_j = \frac{\lambda_j}{\sum_{i=1}^{N_p} \lambda_i} \tag{8}$$

Figure 10 shows the cumulative energies that the modes occupy, which are arranged from the value with the largest energy ratio. In this study, the desired cumulative energy is set 99.999% of the total energy. It can be confirmed that only nine and eleven modes (basis vector) are required for β and h_c, respectively, to depict the set cumulative energy. Three of the POD modes, which have the largest energy ratios of β and h_c are presented above leading-edge extent (x/c_0 = -0.016 – 0.008, c_0: full-scale airfoil chord), as shown in Fig.11. In the case of POD mode 1, the energy ratios of β and h_c are estimated to be approximately 97.2 % and 96.3 %, respectively, as shown in Fig. 10. It is expected that they best represent the tendency of the snapshots. It can also be confirmed from Fig. 11 that POD mode 1 best describes the general β and h_c shapes. POD modes 2 and 3 are expected to be used to adjust the overall variance, including moving POD mode 1 left and right. The POD coefficients are obtained by projecting the snapshots onto the POD modes. Then, the POD coefficients are interpolated on the design surface by kriging. For the stagnation point location, one scalar data point is interpolated.

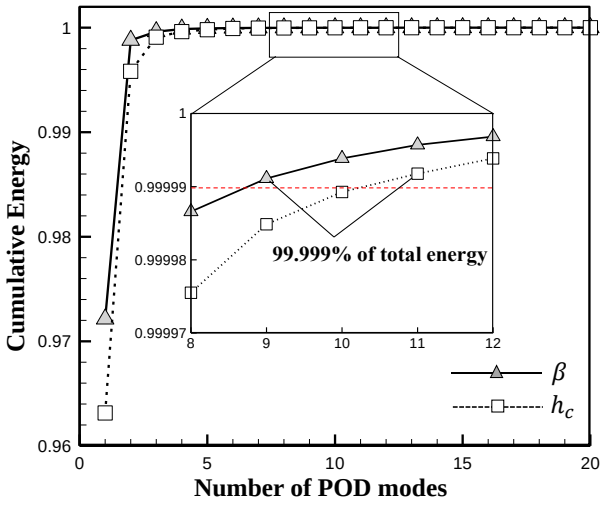

Fig. 10 Cumulative energy of the number of POD modes

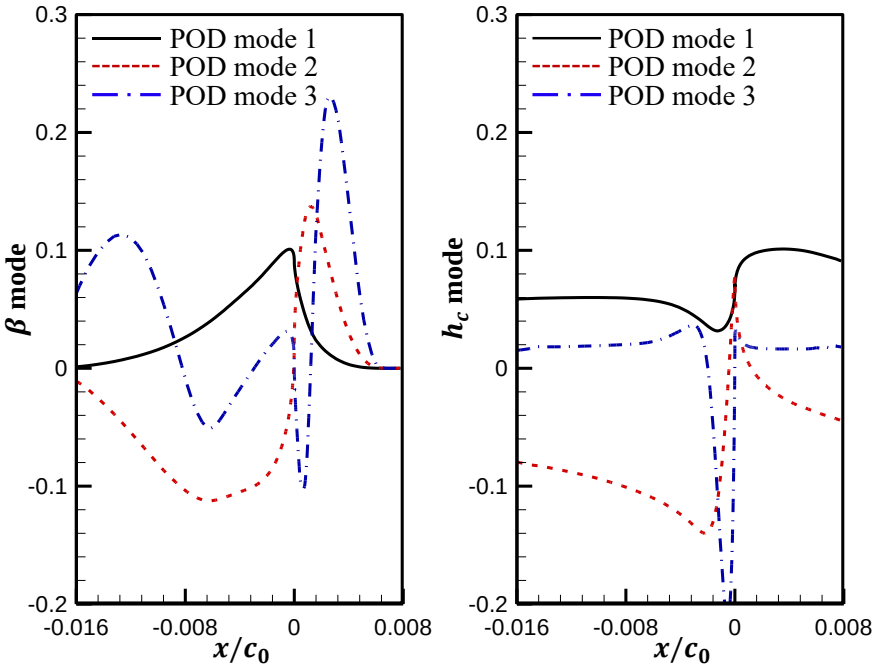

317

318 **Fig. 11 POD modes of the β (left) and h_c(right)**

319 Next, leave-one-out cross-validation (LOOCV) is used to evaluate ROM accuracy. The LOOCV error is
320 calculated by removing one snapshot from the whole snapshot, creating a ROM, and calculating the difference
321 between the predicted value (prediction by ROM) and the original value (CFD solution) at the point, as follows:

$$LOOCV\ \varepsilon = \varepsilon_1 + \varepsilon_2$$
$$\varepsilon_1 = \left\| U_{CFD,\beta} - V_{ROM,\beta} \right\|_2,\ \varepsilon_2 = \left\| U_{CFD,h_c} - V_{ROM,h_c} \right\|_2 \tag{9}$$

322 The LOOCV error (ε) is the sum of the LOOCV errors of β and h_c, which are the values at the optimum
323 values obtained from the ROM, and each parameter is normalized. Until the LOOCV error (ε) satisfies the
324 minimum error (0.1), sample points are repeatedly added. The adaptive sampling presented in the Appendix is
325 used to determine additional sample points which are the largest values from the formulation ($MMSE(x) =$
326 $\varphi(x)^\rho \sigma_n^2(x),\ \varphi(x) = \varepsilon_{LOOCV}(\beta) \times \varepsilon_{LOOCV}(h_c)$). GA is used to find the largest value and seven sample points are
327 added in each iteration. For the weight function (ρ), 0 is used for 2 points, 1 is used for the other two points, and
328 3 is used for the other two points. The optimum point of the ROM is selected as the last sample point.

329

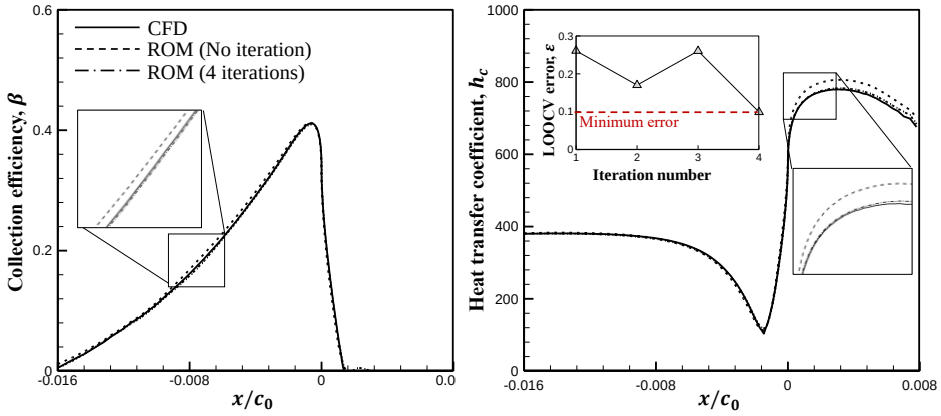

Fig. 12 Change of LOOCV error, β and h_c after 3 iteration through adaptive sampling, ($V_\infty = 102.8m/s$, $\alpha = 2°$, LWC $= 2.4g/m^3$, MVD $= 18\mu m$, $T_\infty = 263.15K$)

Figure 12 shows the change in LOOCV error (ε), β, and h_c values predicted from ROM for one initial sample point where the error was large, after repeating the adaptive sampling a total of four times. It is confirmed that the difference between the CFD and ROM values of β and h_c decreases, respectively and the LOOCV error (ε) satisfies the minimum error (0.1) with four iterations. Therefore, the kriging model is assumed to converge after four refinement iterations, with 28 added sample points.

Once the kriging model converges, an optimal solution is obtained. The minimum errors ($\varepsilon_{min,\beta}$, ε_{min,h_c}) are set to 0.02, and optimization is performed via GA. From the optimization results, the geometries, ice shapes, and distributions of β and h_c of the full-scale and hybrid airfoils are presented in Fig.13. Note that all of the values of the hybrid airfoil are in good agreement with the values of the full-scale airfoil.

The hybrid and full-scale airfoils have chord lengths of 1.458 m and 3.07 m, respectively. The hybrid scale factor is 2.11, which indicates that the hybrid airfoil chord is more than twice as short as the full-scale airfoil chord. The thickness decreases from 0.352 to 0.273 m, which is an important factor in determining the collection efficiency [19]. In this study, the hybrid airfoil has smaller leading-edge curvature than that of the full-scale airfoil, so the leading-edge thickness is larger than that of the full-scale airfoil. Therefore, although the total thickness of the hybrid airfoil is smaller than that of the full-scale airfoil, an accurate distribution of β can be obtained owing to the influence of the leading-edge thickness. This is important because if the thickness increases to obtain a similar full-scale β, it will be difficult to make a shorter hybrid airfoil owing to the large separation, which results

from the increased curvature of the aft section.

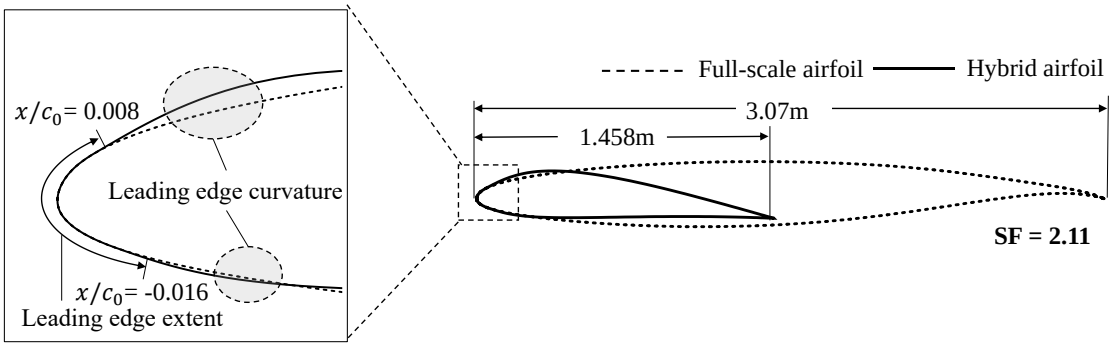

a) Geometries of hybrid airfoil and full-scale airfoil

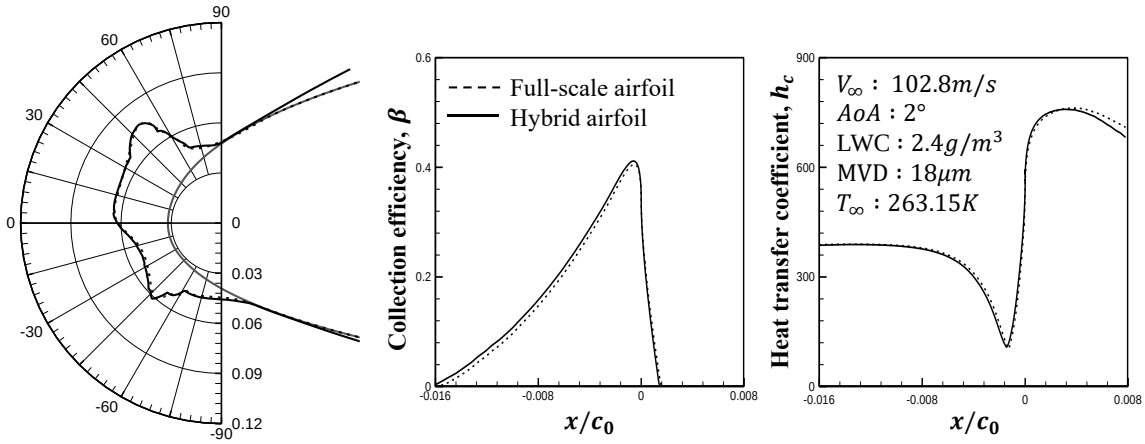

b) Comparison of ice shape (left), collection efficiency (middle) and heat transfer coefficient (right)

Fig. 13 Comparison of geometries, ice shapes, collection efficiency and heat transfer coefficient of hybrid airfoil and full-scale airfoil

The leading-edge curvature is designed considering all the geometric effects of the hybrid airfoil to match distributions of not only full-scale β but also full-scale h_c. The necessity of comprehensively considering β and h_c is explained in detail in the next section.

B. The necessity of matching the distribution of collection efficiency and heat transfer coefficient

In this study, to design a compact hybrid airfoil, which can be applied in glaze ice conditions with high LWC and temperature, the full-scale stagnation point location, as well as the distributions of full-scale β and h_c, are directly matched. To demonstrate the necessity of each parameter, three cases are selected as listed in Table 3. Only the stagnation point locations are matched for the first case, and the stagnation point locations and distributions of β are matched for the second case, and stagnation point locations and distributions of β and h_c

364 are matched for the third case. In each case, the hybrid airfoil has a scale factor of 2 or more.

365 **Table 3 Test cases**

Case number	1	2	3
Stagnation point	Match	Match	Match
Distribution of β	No match	Match	Match
Distribution of h_c	No match	No match	Match

366

367 A comparison of the flow fields, distributions of β and h_c between the full-scale and hybrid airfoils of the
368 cases are presented in Fig.14. In case 1, the thickness of the hybrid airfoil is 50% of the full-scale thickness.
369 Therefore, β of the hybrid airfoil presents an 11 % higher peak of full-scale β and the suction side of hybrid
370 airfoil has a larger curvature than that of the other hybrid airfoils. A high flow velocity is formed on the suction
371 side of the airfoil, which affects the boundary layer and increases h_c owing to the large curvature. As a result,
372 h_c on the leading-edge extent has an 11.4 % higher peak of full-scale h_c. In case 2, the thickness of the hybrid
373 airfoil is 75 % that of the full-scale thickness. However, as mentioned before, because the hybrid airfoil has a
374 smaller leading-edge curvature and larger leading-edge thickness than those of the full-scale airfoil, it is possible
375 to achieve the same distribution of full-scale β. h_c of the hybrid airfoil has an 8 % lower peak of the full-scale
376 h_c. This is because this case does not consider the variance of the distribution of h_c due to the different aft section
377 geometry including the leading-edge curvature and the viscous effect of separation. On the other hand, the hybrid
378 airfoil in case 3 has an 75 % thickness of full-scale airfoil, same with case 2, but it is designed considering not
379 only distributions of β but also h_c. Therefore, both distributions can be matched with those of the full-scale
380 airfoil.

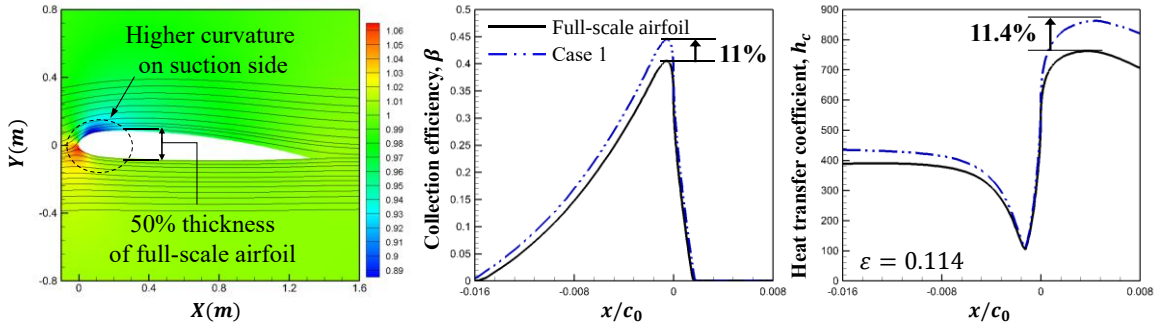

a) Case 1 : Flow field (left), collection efficiency (middle) and heat transfer coefficient (right)

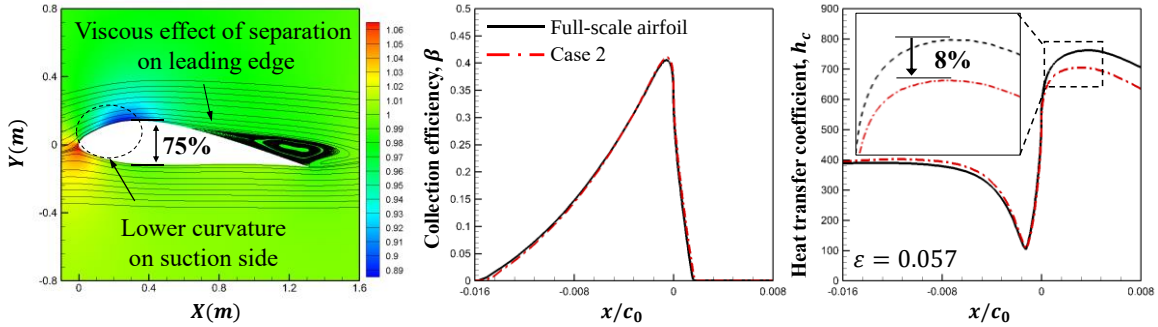

b) Case 2 : low field (left), collection efficiency (middle) and heat transfer coefficient (right)

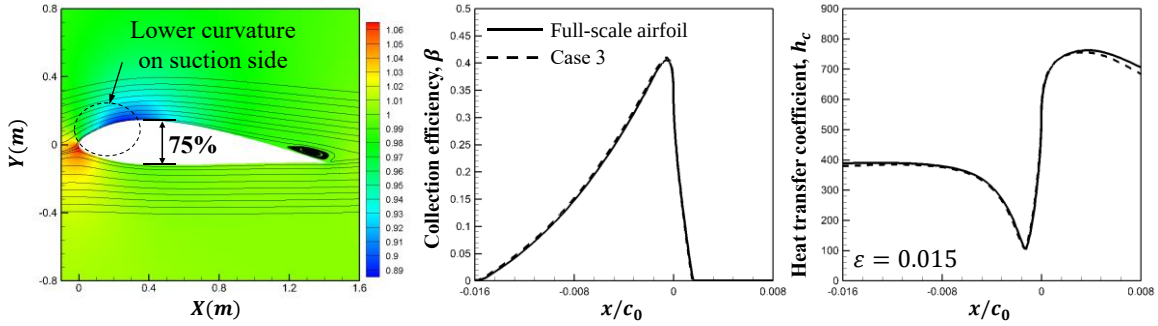

c) Case 3 : Flow field (left), collection efficiency (middle) and heat transfer coefficient (right)

Fig. 14 Comparison of each case when matching stagnation point, stagnation point with distribution of β and stagnation point with distribution of β and h_c

Figure 15 compares an analysis of the ice shapes of the three cases with the full-scale ice shape. The ice shapes of each case are analyzed using the three methods. First is the different area ratio between the ice shapes of full-scale and hybrid airfoils, which are different ice shape areas divided by the full-scale ice area. Second, the angle difference of the ice horns is calculated. Finally, the difference in the length of the ice horn divided by the full-scale ice horn length is defined. The angle and length of the ice horn are calculated by the leading-edge center of the full-scale airfoil.

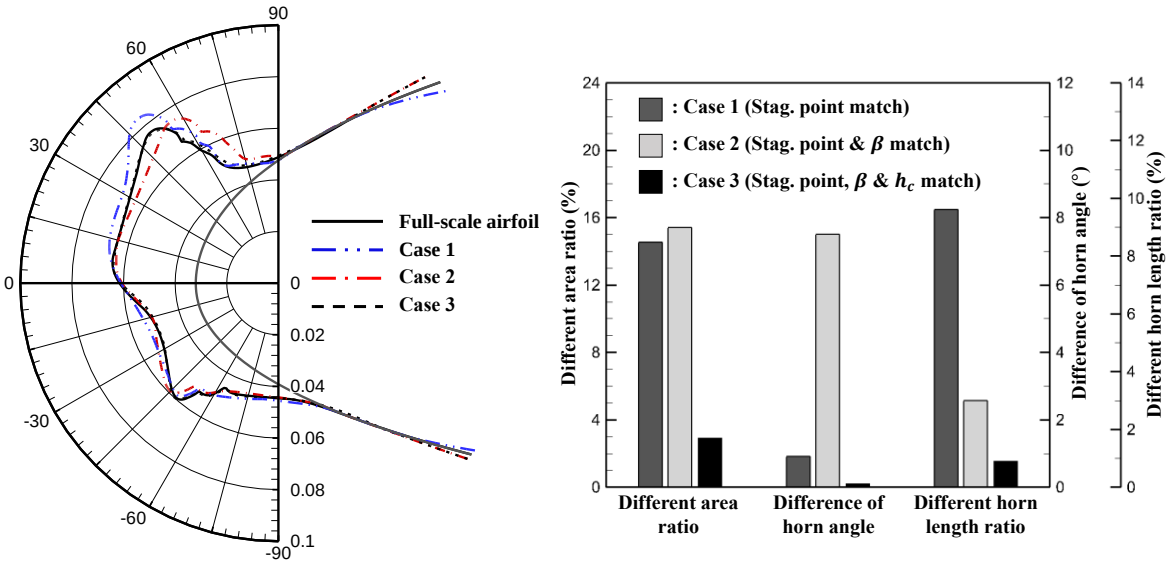

Fig. 15 Radial ice shapes (left) and ice shape analysis (right) for cases

In case 1, no specific difference in horn angle is observed because both distributions of β and h_c are over-predicted compared to those of the full-scale airfoil. However, significant differences are observed at different area ratios and horn length ratios of, 14.53 % and 9.6 %, respectively. In case 2, it is confirmed that the ice accretes less on the leading-edge side and the remaining water runs back, so the ice horn is formed at a different angle from the full-scale ice horn. Different area ratios and differences of horn angle, 7.5 ° and 15.4 %, respectively are observed. This is because the distribution of β is matched with full-scale β but h_c has a lower peak than full-scale h_c. On the other hand, the ice shape of case 3 is in good agreement with the full-scale ice shape. It can be confirmed that case 3 is highly accurate in all aspects, including a different area ratio of 3% or less. The results indicate that considering all parameters simultaneously is required to improve the performance of the hybrid airfoil in this case.

The icing wind tunnel test is performed using a hybrid airfoil instead of a full-scale airfoil and hence the ice shape of the hybrid airfoil must have sufficient reliability. For more reliable test results, it is necessary to minimize the error in the numerical analysis. Therefore, the method of matching not only the full-scale stagnation point location but also the distributions of full-scale β and h_c are highly recommended for glaze ice conditions with high LWC and temperature.

C. Effects of relaxing the constraint of separation

In this study, a viscous turbulent CFD-icing simulation is used to relax the separation constraint. This section presents the difference between chord lengths of a hybrid airfoil when designed to allow separation and when designed to apply a separation constraint. Both airfoils are designed using the same design process, with the same constraint values, except for allowing separation. The flow fields are shown in Figs. 16 (a) and (b). It can be confirmed that the hybrid airfoil can be designed even though separation occurs by allowing separation.

A comparison of the hybrid airfoil geometries is shown in Fig. 16 (c). The hybrid airfoil applying the separation constraint has a 1.69 m chord and the hybrid airfoil allowing separation has a 1.458m chord. This is the result of reducing the 1.69 m hybrid airfoil by approximately 13.7 %. The hybrid scale factor also increases from 1.8 – 2.1. The result indicates that more compact hybrid airfoil can be designed by relaxing the constraint. Furthermore, it is also possible to eliminate unnecessary processes to check the occurrence of separation.

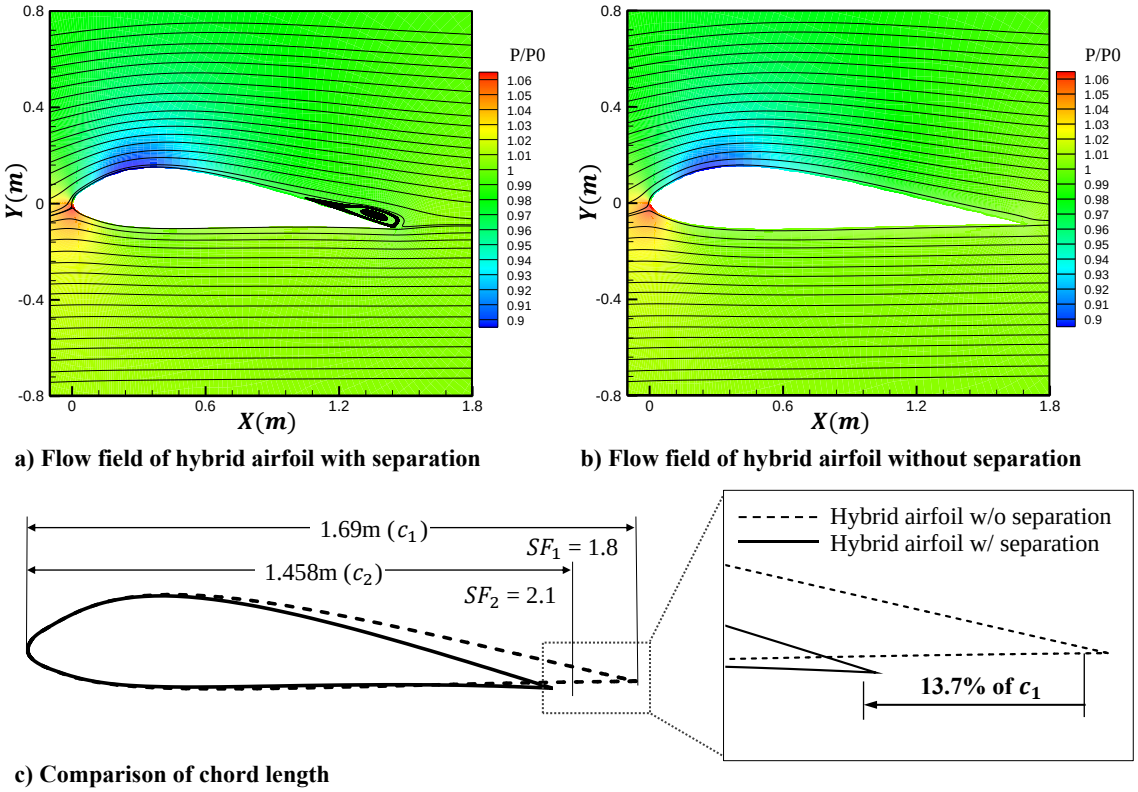

a) Flow field of hybrid airfoil with separation

b) Flow field of hybrid airfoil without separation

c) Comparison of chord length

Fig. 16 Comparison of the flow field and chord length of hybrid airfoil designed with and without separation ($V_\infty = 102.8m/s$, $\alpha = 2°$, LWC $= 2.4g/m^3$, MVD $= 18\mu m$, $T_\infty = 263.15K$)

D. General optimization design method for flap geometry

Single-element hybrid airfoil that can be applied to only one angle of attack has the advantage of a relatively simple hybrid airfoil geometry definition. However, for practical application, it is desirable to design the hybrid airfoil to cover every angle of attack. Through a flap, it is possible to design a hybrid airfoil that can be applied to multiple angles of attack. The use of a flap can reduce the size of separation [17] and the occurrence of unsteadiness due to separation. In this study, a slotted flap generally, which is generally used to reduce separation, is selected. The geometries of the main section and flap are designed using the optimization design process presented earlier.

The purpose of this section is to design the hybrid airfoil with a slotted flap to be applied to angles of attack (α) from 0 to 5 °. The single-element hybrid airfoil is designed as a reference geometry for flap design at an angle of attack of zero. The leading-edge extent of the single-element hybrid airfoil includes all ranges of ice accretions that occur from α = 0 ° to α = 5 °. Then, the aft section is designed to minimize the chord. The main section and flap from the single-element hybrid airfoil are designed using the same design process presented in Fig. 3. Using OLHS, 70 initial sample points for seven design variables are selected, and the ROM of β and h_c is constructed. Based on the ROM, the optimization is conducted with the following formulation.

$$\text{minimize} \quad \sum(\varepsilon_{\beta(x)} \times \varepsilon_{h_c(x)}) \tag{10}$$

$$\text{subject to} \quad x \in \Omega \tag{11}$$

where

$$\varepsilon = \int_{LE} \left| U_{full} - V_{hybrid} \right| ds \Big/ \int_{LE} U_{full} ds \quad (U, V \in \mathbb{R}^{N_p}) \tag{12}$$

The objective function is to minimize the sum of the error ($\varepsilon_{\beta(x)} \times \varepsilon_{h_c(x)}$), which are calculated at α = 0 °, 3 °, and 5 °. The error is the value obtained from the optimal flap deflection angle (δ), which is adjusted, for each geometry. The deflection angle is calculated from the reference geometry in the counterclockwise direction. The constraint is that the design variables must exist in the region (denoted as Ω) where unsteadiness does not occurs as presented previously.

Figure 17 shows the geometry of the flaps, ice shapes and flow fields of the optimal hybrid airfoil at α = 0°, 3° and 5°. It can be seen that the main section and flap are obtained from the reference geometry. The deflection angles are -3.7 °, 8.2 °, and 13.3 ° at α = 0 °, 3 °, and 5 °, respectively. The ice shapes of the hybrid airfoils are in good agreement with the full-scale ice shapes at each angle of attack; this is because the optimal flap and main section are designed through optimization, considering all flow effects of those geometries, such as separation. As a result, when the flap and the main section are designed using the general method presented in this study, the ice shapes can be accurately matched with full-scale ice shapes even at multiple angles of attack.

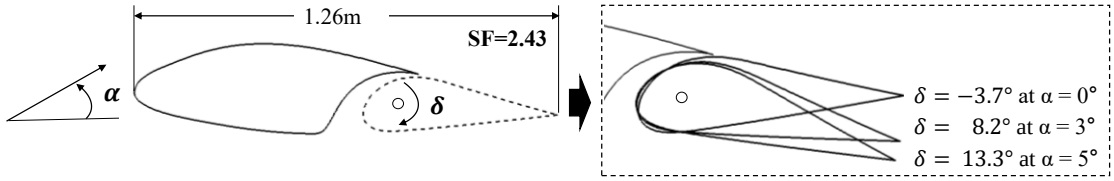

a) Hybrid airfoil with single slotted flap (left) and flap deflection angle at each angle of attack (right)

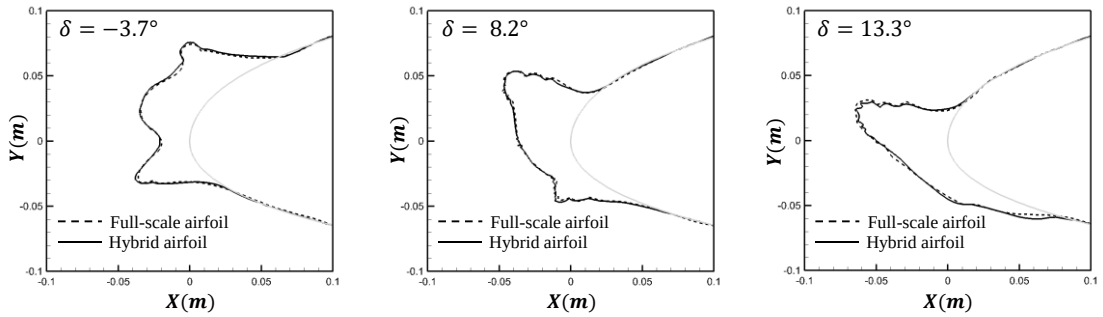

b) Comparison of ice shapes at $\alpha = 0^{\circ}$(left), $\alpha = 3^{\circ}$(middle) and $\alpha = 5^{\circ}$(right)

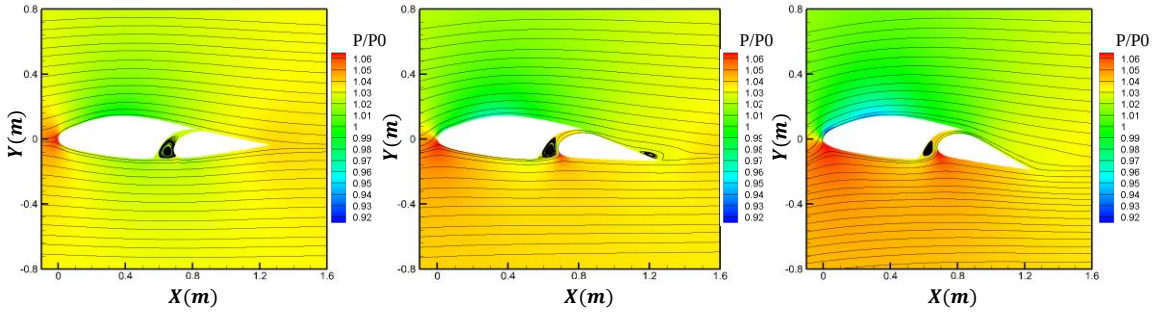

c) Flow field of hybrid airfoil at $\alpha = 0^{\circ}$(left), $\alpha = 3^{\circ}$(middle) and $\alpha = 5^{\circ}$(right)

Fig. 17 Main section and flap geometry with deflection angle at α = 0°, 3° and 5°, ($V_{\infty} = 102.8m/s$, $\alpha = 2°$, LWC $= 2.4g/m^3$, MVD $= 18\mu m$, $T_{\infty} = 263.15K$)

IV. Conclusions

The purpose of the present study was to provide a general method for designing a compact hybrid airfoil that can be applied to glaze ice conditions with high LWC and temperature. To improve accuracy, the full-scale stagnation point location used in previous studies, as well as the distributions of full-scale collection efficiency (β) and heat transfer coefficient (h_c), were directly matched. For computational efficiency, reduced-order modeling (ROM)-based optimization was applied to match the distributions of full-scale β and h_c. The optimization design process was applied to a glaze ice condition with high LWC and temperature. As a result of the thorough investigation, the following conclusions were reached:

1) By directly matching the stagnation point location and distributions of β and h_c with those of full-scale airfoil, it was possible to design an optimal hybrid airfoil in glaze ice conditions, where a substantial amount of water run-back occurs. The proposed approach simultaneously considers the variations in the distributions of h_c and β as well as stagnation point location, owing to the effects of the aft section geometry, including the leading-edge curvature and the separation. Therefore, in a glaze ice condition, the agreement rate of ice shapes between the full-scale and hybrid airfoils could be significantly improved. The results indicate that it is highly recommended to match the distribution of h_c as well as β to minimize the error between full-scale and hybrid airfoil ice shapes to obtain more reliable results from icing tunnel tests for the glaze ice conditions.

2) By allowing separation, the hybrid airfoil obtained a more compact size than that designed without separation. The hybrid airfoil has a condition in which separation is likely to occur because the aft section of the hybrid airfoil is shorter than that of the full-scale airfoil. Therefore, designing the hybrid airfoil so that separation does not occur is an excessive constraint on the design space. In this study, a hybrid airfoil can be designed with separation by viscous turbulent CFD icing simulations. In addition, the constraint on unsteadiness was set. When applied to the icing condition, the hybrid airfoil could be designed as 11% more compact than the hybrid airfoil designed without separation.

3) Through the presented optimization design process, the ice shape of the hybrid airfoil with the flap yielded good agreement with the full-scale ice shape at various angles of attack. From the single-element hybrid airfoil, the main section and flap were defined using five design variables. From ROM based optimization, the optimal flap and main section geometries were obtained by minimizing the difference in β and h_c

between full-scale and hybrid airfoils. As a result, the flap and main section were designed to generate accurate full-scale ice shapes at each angle of attack.

The present study is limited to the design of a hybrid airfoil in conventional supercooled droplet case and no heating mode. Further study on the effects of supercooled large droplet (SLD) defined in Appendix O and the presence of anti-icing system is needed. In addition, the method of matching the distribution of parameter through ROM needs to be applied and extended to design a 3D hybrid wing. We hope to report the investigation of these subjects in the future.

Appendix: Adaptive sampling

It is widely known that the quality of surrogate model-based approximations such as ROM is critically affected by snapshots. In particular, the POD-based ROM, which comprises a linear combination of basis vectors, cannot offer accurate reduced-order solutions when there is a nonlinear problem or insufficient information of snapshots. To solve this problem, an adequate number and location of snapshots should be chosen. For computational efficiency, it is necessary to create a sufficiently accurate model for as few snapshots as possible. However, it is difficult to know in advance how many snapshots are needed and the best snapshot locations. Therefore, a method that continuously adds snapshots using the information obtained from the previous model is required.

In this study, the adaptive sampling method [32], which can use the leave-one-out cross-validation (LOOCV) error and snapshot variance, is adopted as a method of adding snapshots. Among them, the maximum mean squared error (MMSE) approach, where LOOCV error and normalized predictive variance can be expressed in one score function is used; this is formulated as follows:

$$MMSE(x) = \varphi(x)^{\rho}\sigma_n^2(x),\ \varphi(x) = \varepsilon_{LOOCV}(\beta) \times \varepsilon_{LOOCV}(h_c) \tag{A1}$$

where

$$\varepsilon_{LOOCV}^{i} = \left\| U_{CFD}^{i} - U_{ROM}^{i} \right\|_2 ,\ U \in \mathbb{R}^{N_p}, i = 1, \dots, N_s \tag{A2}$$

ρ is used as a weight factor to adjust the ratio of the LOOCV error and the normalized predictive variance in the system.

$\varphi(x)$ represents the LOOCV error and the value is calculated by multiplying the LOOCV errors of β and h_c.

The Voronoi cell is applied to all domains and the LOOCV error corresponding to the sample point is used for the Voronoi region associated with the point. The LOOCV error contains information about the deviation of the surrogate model. If the region has a large LOOCV error, it can be judged that a nonlinear feature occurs. To reduce error, local exploitation is recommended in such regions through the weight factor.

$\sigma_n^2(x)$ is a value indicating the normalized predictive variance of x, which is the point in the input domain. The specific formulation can be found in reference to [32]. The normalized predictive variance is the quantified value of closeness from all other sample points. Therefore, if a particular point shows a large variance value, it can be determined that it is "under-sampled" in the current input domain. By adding new sample points with global exploration, this variance can be reduced.

Acknowledgements

This work was supported by the National Research Foundation of Korea (NRF) Grant funded by the Ministry of Science and ICT (NRF-2017R1A5A1015311).

References

[1] Jeck, R. K., "Icing Design Envelopes (14 CFR Parts 25 and 29, Appendix C) Converted to a Distance-Based Format," Federal Aviation Administration TR DOT/FAA/AR-00/30, Atlantic City, NJ, 2002.

[2] Federal Aviation Regulations Part 25: Airworthiness Standards Transport Category Airplanes, Federal Aviation Administration, U S Government Printing Office Washington D C June 1974 (revised edition, May 1982).

[3] "FAA Inflight Aircraft Icing Plan," Federal Aviation Administration, U.S. Department of Transportation, Washington D.C., April 1997.

[4] Bragg, M., Gregorek, G., and Shaw, R., "An Analytical Approach to Airfoil Icing," *19th Aerospace Sciences Meeting*, AIAA Paper 1981-0403, 1981.doi:10.2514/6.1981-403

[5] Bragg, M. B., "Effect of Geometry on Airfoil Icing Characteristics," *Journal of Aircraft*, Vol. 21, No. 7, 1984, pp. 505–511.doi:10.2514/3.45000

[6] Ruff, G., "Verification and Application of the Icing Scaling Equations," *24th Aerospace Sciences Meeting*, AIAA Paper 1986-0481, 1986.doi:10.2514/6.1986-481

[7] Bilanin, A. J., "Proposed Modifications to Ice Accretion/Icing Scaling Theory," *Journal of Aircraft*, Vol. 28, No. 6, 1991, pp. 353–359.doi:10.2514/3.46034

[8] Anderson, D., "Rime-, Mixed- and Glaze-Ice Evaluations of Three Scaling Laws," *32nd Aerospace Sciences Meeting and Exhibit*, AIAA Paper 1994-0718, 1994. doi:10.2514/6.1994-718

[9] Anderson, D., "Methods for Scaling Icing Test Conditions," *33rd Aerospace Sciences Meeting and Exhibit*, AIAA Paper 1995-0540, 1995. doi:10.2514/6.1995-540

[10] Saeed., F., Selig, M. S., and Bragg, M, B., "Design of Subscale Airfoils with Full-Scale Leading Edges for Ice Accretion Testing", *Journal of Aircraft*, Vol. 34, No. 1, 1997, pp. 94-100. doi.org/10.2514/2.2140

[11] Von Glahn, U. H., "Use of Truncated Flapped Airfoils for Impingement and Icing Tests of Full-Scale Leading-Edge Sections," NACA RME56E11, 1956.

[12] Langmuir, I., and Blodgett, K. B., "A Mathematical Investigation of Water Droplet Trajectories," Army Air Forces Tech. Rept. 5418, Dayton, OH, 1946.

[13] Hauger, H., and Englar, K., "Analysis of Model Testing in an Icing Wind Tunnel," Douglas Aircraft Company, Inc. Rept. SM-14993, May 1954.

[14] Sibley, E., and Smith, R., "Model Testing in an Icing Wind Tunnel," Lockheed Aircraft Corp. Rept. LR-10981, 1955.

[15] Saeed, F., Selig, M. S., and Bragg, M. B., "Hybrid Airfoil Design Method to Simulate Full-Scale Ice Accretion Throughout a Given α Range," *Journal of Aircraft*, Vol. 35, No. 2, 1998, pp. 233–239. doi:10.2514/2.2289

[16] Saeed, F., Selig, M. S., and Bragg, M. B., "Hybrid Airfoil Design Procedure Validation for Full-scale Ice Accretion Simulation," *Journal of Aircraft*, Vol. 36, No. 5, 1999, pp. 769–776. doi.org/10.2514/2.2532

[17] Fujiwara, G. E., and Bragg, M. B., "Method for Designing Hybrid Airfoils for Icing Wind-Tunnel Tests," *Journal of Aircraft*, Vol. 56, No. 1, 2019, pp. 137-149.

[18] Fujiwara, G. E., and Bragg, M. B., "Method for Designing 3D Swept Hybrid Wings for Icing Wind-Tunnel Tests," *Journal of Aircraft*, Vol. 56, No. 2, 2019, pp. 730–746. doi.org/10.2514/1.C035136

[19] Fujiwara, G., Bragg, M., Triphahn, C., Wiberg, B., Woodard, B., Loth, E., Malone, A., Paul, B., Pitera, D., and Wilcox, P., et al., "Development of Experimental Icing Simulation Capability for Full Scale Swept Wings: Hybrid Design Process, Years 1 and 2," NASA CR-2017-219573, 2017.

[20] Wright,W., "User's Manual for LEWICE Version 3.2," NASA CR-2008- 214255, 2008.

560 [21] Ruff, G. A., and Berkowitz, B. M., “User’s Manual for the NASA Lewis Ice Accretion Prediction Code
561 (LEWICE),” NASA CR-185129, 1990.
562 [22] Loéve, M., Probability Theory, Van Nostrand, New York, 1967, pp. 166–178.
563 [23] Holmes, P., Lumley, J. L., and Berkooz, G., Turbulence, Coherent Structures, Dynamical Systems and
564 Symmetry, Cambridge Univ. Press, Cambridge, England, U.K., 1996, pp. 68–100.
565 [24] Bui-Thanh, T., Damodaran, M., and Willcox, K., “Proper Orthogonal Decomposition Extensions for
566 Parametric Applications in Compressible Aerodynamics,” *21st AIAA Applied Aerodynamics Conference*, AIAA
567 Paper 2003-4213, 2003.
568 [25] Fossati, M., and Habashi, W. G., “Multiparameter Analysis of Aero Icing Problems Using Proper Orthogonal
569 Decomposition and Multidimensional Interpolation,” *AIAA Journal*, Vol. 51, No. 4, 2013, pp. 946–960.
570 doi:10.2514/1.J051877
571 [26] Nakakita, K., Nadarajah, S., and Habashi, W., “Toward Real-Time Aero-Icing Simulation of Complete
572 Aircraft via FENSAP-ICE,” *Journal of Aircraft*, Vol. 47, No. 1, 2010, pp. 96–109. doi:10.2514/1.44077
573 [27] Zhan, Z., Habashi, W. G., and Fossati, M., “Local Reduced-Order Modeling and Iterative Sampling for
574 Parametric Analyses of Aero-Icing Problems,” *AIAA Journal*, Vol. 53, No. 8, 2015, pp. 2174–2185.
575 doi:10.2514/1.J053654
576 [28] Zhan, Z., Habashi, W. G., and Fossati, M., "Real-Time Regional Jet Comprehensive Aero icing Analysis via
577 Reduced Order Modeling", *AIAA Journal*, Vol. 54, No. 12, 2016, pp. 3787-3802.
578 [29] Sacks, J., Welch, W. J., Mitchell, T. J., and Wynn, H. P., “Design and Analysis of Computer Experiments,”
579 *Statistical Science*, Vol. 4, No. 4, 1989, pp. 409–435.
580 [30] Park, J.-S., “Optimal Latin-Hypercube Designs for Computer Experiments,” *Journal of Statistical Planning*
581 *and Inference*, Vol. 39, No. 1, 1994, pp. 95–111.
582 [31] Martin, J. D., and Simpson, T. W., “Use of Kriging Models to Approximate Deterministic Computer Models,”
583 *AIAA Journal*, Vol. 43, No. 4, 2005, pp. 853–863.
584 [32] Kyprioti, A. P., Zhang, J., and Taflanidis, A. A., “Adaptive Design of Experiments for Global Kriging
585 Metamodeling through Cross-validation Information,” *Structural and Multidisciplinary Optimization*, 2020, 1-23.
586 [33] Jones, D. R., “A Taxonomy of Global Optimization Methods Based on Response Surfaces,” *Journal of Global*
587 *Optimization*, Vol. 21, No. 4, 2001, pp. 345–383. doi:10.1023/A:1012771025575

588 [34] Du, Q., Faber, V., and Gunzburger, M., "Centroidal Voronoi Tessellations: Applications and Algorithms,"
589 SIAM Review, Vol. 41, No. 4, 1999, pp. 637–676. doi:10.1137/S0036144599352836
590 [35] Son, C., Oh, S., and Yee, K., "Ice Accretion on Helicopter Fuselage Considering Rotor-Wake Effects,"
591 *Journal of Aircraft*, Vol. 54, No. 2, 2017, pp. 500–518. doi:10.2514/1.C033830
592 [36] Son, C., and Yee, K., "Procedure for Determining Operation Limits of High-Altitude Long-Endurance
593 Aircraft Under Icing Conditions," *Journal of Aircraft*, Vol. 55, No. 1, 2018, pp. 294–309.
594 doi.org/10.2514/1.C034490
595 [37] Min, S., and Yee, K. (2020). New Roughness-Induced Transition Model for Simulating Ice Accretion on
596 Airfoils. *AIAA Journal*, 1-13. doi.org/10.2514/1.J059222
597 [38] Park, S. H., and Kwon, J. H., "Implementation of *k-w* Turbulence Models in an Implicit Multigrid
598 Method," *AIAA Journal*, Vol. 42, No. 7, 2004, pp. 1348-1357.
599 [39] Allmaras, S. R., Johnson, F. T., and Spalart, P. R., "Modifications and Clarifications for the Implementation
600 of the Spalart–Allmaras Turbulence Model," *7th International Conference on Computational Fluid Dynamics*,
601 ICCFD7-1902, Big Island, HI, June 2012.
602 [40] Jung, S. K., Myong, R. S., and Cho, T. H., "Development of Eulerian Droplets Impingement Model Using
603 HLLC Riemann Solver and POD-based Reduced Order Method," *41st AIAA Fluid Dynamics Conference and*
604 *Exhibit*, American Institute of Aeronautics and Astronautics, 2011.
605 [41] Jung, S. K., and Myong, R. S., "A Second-Order Positivity-Preserving Finite Volume Upwind Scheme for
606 Air-Mixed Droplet Flow in Atmospheric Icing," *Computers & Fluids*, Vol. 86, 2013, pp. 459-469.
607 [42] Jung, S. K., and Myong, R. S., "A Relaxation Model for Numerical Approximations of the Multidimensional
608 Pressureless Gas Dynamics System," *Computers and Mathematics with Applications*, Vol. 80, No. 5, 2020, pp.
609 1073-1083.
610 [43] Wright, W. B., and Rutkowski, A., "Validation Results for LEWICE 2.0," NASA CR-1999-208690, 1999.
611 [44] Vassberg, J., Dehaan, M., Rivers, M., and Wahls, R., "Development of a Common Research Model for
612 Applied CFD Validation Studies," *26th AIAA Applied Aerodynamics Conference*, AIAA Paper 2008-6919, Aug.
613 2008.doi:10.2514/6.2008-6919.